Multifrequency and Multiload WPT System Based on Cascade H-Bridge Multilevel Inverter

Chenyang Xia, *Member, IEEE*, Tao Lu, Ganquan Cui, Anran Sun, Xinheng Li, Xirui Wang, and Yan Sun

***Abstract*—To address the issues of limited output power and harmonic interference in existing multifrequency and multiload magnetic coupling resonant wireless power transfer (MFML-MCR-WPT) systems, this article proposes a MFML-MCR-WPT system based on a cascaded H-bridge multilevel inverter (CHB-MLI). The system utilizes the phase disposition multifrequency modulation technique, achieving arbitrary frequency and quantity power output and control through the design of modulation wave quantity, frequency, and amplitude. First, the structure of the CHB-MLI-based MFML-MCR-WPT system is proposed, and the working principle of the multifrequency modulation method is analyzed. Subsequently, a five-level dual-frequency and dual-load system is taken as an example to establish the mathematical model. Then, system parameter optimization is conducted to suppress cross-coupling and interfrequency interference. Furthermore, to address the power and loss imbalance among H-bridge units under multifrequency low modulation indices, a carrier reconstruction method is adopted to balance power distribution and switching losses. Finally, an experimental platform is constructed to validate the proposed theory. Simulation and experimental results demonstrate that the system achieves multilevel multifrequency power output with continuous power and frequency control, maintains minimal interchannel interference, and achieves H-bridge unit balancing ratios of 1:1.19, while exhibiting excellent system compatibility and controllability.**

***Index Terms*—Carrier reconstruction, cascaded H-bridge multilevel inverters (CHB-MLI), multifrequency and multiload magnetic coupling resonant wireless power transfer (MFML-MCR-WPT), phase disposition multifrequency modulation.**

I. INTRODUCTION

MAGNETIC coupling resonant wireless power transfer (MCR-WPT) technology has been extensively studied and applied in electric vehicles [1], drones [2], underwater equipment [3], portable devices [4], and implantable medical devices [5], owing to its contactless energy transmission capability between power sources and receivers, which ensures enhanced charging safety, operational convenience, and system flexibility.

Multifrequency and multiload wireless power transfer (MFML-WPT) systems have attracted significant research attention due to their capability to simultaneously deliver multifrequency power to multiple loads. Current research on MFML-WPT technology primarily focuses on: multifrequency power generation, power distribution control, decoupled coil design, multifrequency resonant network synthesis, and system parameter identification. Significant research efforts have been conducted on multifrequency power generation, yielding established methodologies that can be categorized into: stacked inverter configurations, harmonic utilization schemes, time-division multiplexing approaches, and various multifrequency modulation strategies.

1) The stacked inverter configuration achieves multifrequency power output through superposition of multiple inverters operating at distinct frequencies. As demonstrated by Liu et al. [6], two independent inverters generating different frequency outputs were implemented, with energy transmission realized through dedicated transmitting coils. In [7], the outputs of half-bridge inverters operating at different frequencies were superimposed on a shared transmitting coil via multiple transformers, where power distribution is regulated by controlling the value of the primary-side capacitor C_{p}.
2) The harmonic utilization scheme leverages the fundamental and harmonic components of inverter outputs to achieve multifrequency power transmission. As demonstrated by Liu et al. [8], superposition of the fundamental component with the fifth and seventh harmonic components was implemented, enabling a single transmitting coil to power receiving circuits tuned to corresponding frequencies. Utilizing the sinusoidal component and switching-frequency component in the inductor of a Buck converter, Wang et al. [9] achieved simultaneous wired charging and dual-band wireless power transfer.
3) The time-division multiplexing approach enables multifrequency power delivery by outputting distinct frequencies in different time intervals to satisfy diversified load requirements. As implemented in [10], three receiving circuits with different frequencies were powered in time-allocated slots. This method eliminates interchannel

---

Received 23 May 2025; revised 25 July 2025 and 22 September 2025; accepted 16 November 2025. Date of publication 18 November 2025; date of current version 19 January 2026. This work was supported in part by the National Natural Science Foundation of China under Grant 52277020, in part by the Natural Science Foundation of Jiangsu Province under Grant BK20211246, in part by the Postgraduate Research and Practice Innovation Program of Jiangsu Province under Grant KYCX25_3106, and in part by the Graduate Innovation Program of China University of Mining and Technology under Grant 2025WLJCRCZL356. Recommended for publication by Associate Editor K. Ngo. *(Corresponding author: Chenyang Xia.)*

The authors are with the School of Electrical Engineering, China University of Mining and Technology, Xuzhou 221116, China (e-mail: chyxia@cumt.edu.cn; lutao@cumt.edu.cn; spgqds@cumt.edu.cn; sunar@cumt.edu.cn; lixinheng-@cumt.edu.cn; wangxirui@cumt.edu.cn; ts24230131p31@cumt.edu.cn).

Color versions of one or more figures in this article are available at https://doi.org/10.1109/TPEL.2025.3634405.

Digital Object Identifier 10.1109/TPEL.2025.3634405

interference while achieving power distribution through temporal control.

4) Pulsewidth modulation (PWM) based multifrequency modulation schemes have been extensively explored in recent studies. In [11], a hybrid amplitude-frequency modulation control technique was developed to independently regulate output power across distinct frequencies. Qi et al. [12] proposed a delta-sigma modulated multifrequency approach by synthesizing hybrid-frequency driving voltage pulses from predefined multifrequency components. Further advancements in [13] integrated optimized selective harmonic elimination PWM, effectively reducing switching frequency while maintaining independent voltage control capabilities. A composite modulation wave-based unipolar frequency-doubling method was introduced in [14] for multifrequency energy delivery, with subsequent work in [15] addressing reactive power challenges through a variable resonant network design. Additionally, hysteresis current-tracking modulation in [16] endowed systems with load-agnostic current-source characteristics, while Xia et al. [17] implemented a blocking-delay switching strategy to minimize inverter switching frequency. Furthermore, for this current-source system, a parameter identification method is proposed in [18], enabling precise identification of complex system loads and mutual inductance. Liu et al. [19] utilized a neutral-point-clamped multilevel inverter structure with triangular carrier wave control to achieve independently adjustable multifrequency power output. A neutral-point voltage balancing strategy is incorporated, and a vector control-based approach is proposed for power distribution.

However, through a comprehensive analysis of existing research, it has been identified that current multifrequency power generation methodologies exhibit inherent limitations requiring resolution.

1) *Stacked Inverter Configurations*: The requirement for additional inverters and transmitting coils under multifrequency operation significantly compromises economic viability while increasing system complexity.
2) *Harmonic Utilization Schemes*: The integer multiple relationship between harmonics and the fundamental frequency substantially reduces system compatibility.
3) *Time-Division Multiplexing Approach*: This methodology cannot provide simultaneous power delivery to multiple frequency-specific receiving circuits. As the number of frequencies increases, the power delivery rate decreases proportionally.
4) *Other Multifrequency Modulation Schemes*: Certain implementations employing simplified compensation structures exhibit excessive reactive power, where dynamic reactive power compensation adversely affects active power delivery. Additionally, output power capacity is reduced in some modulation strategies to prevent overmodulation. Furthermore, high computational demands on processors result in suboptimal dynamic performance, particularly manifesting as performance degradation at elevated operating frequencies.

To address the aforementioned limitations, this article proposes a MFML-MCR-WPT system based on cascaded H-bridge multilevel inverter (CHB-MLI) controlled by a hybrid modulation wave phase disposition PWM (HMW-PD-PWM) strategy. The HMW-PD-PWM-controlled CHB-MLI generates superimposed multifrequency power outputs, enabling arbitrary frequency, and arbitrary number configurations. By adjusting the amplitude of modulation waves at different frequencies, independent power control for each frequency is achieved. The power output limitation caused by overmodulation is addressed by increasing the number of H-bridge units in the CHB-MLI topology. Furthermore, a multifrequency resonant compensation (MFRC) network ensures high power factor operation. Simultaneously, a carrier reconstruction mechanism resolves power and loss imbalance among H-bridge units under low modulation indices, thereby enabling independent regulation across a wide power range.

The rest of this article is organized as follows. Section II presents the structure and operating principles of the proposed HMW-PD-PWM controlled MFML-WPT system. Section III establishes the mathematical model of the system, taking a dual-frequency dual-load scenario as an example. Section IV introduces the parameter design methodology for the primary and secondary resonant networks. Based on the designed parameters, Section V analyzes four key characteristics: 1) cross-coupling suppression; 2) interfrequency interference suppression; 3) independent power regulation; and 4) system efficiency. Section VI optimizes the power balance among the H-bridge units of the CHB-MLI inverter under low modulation indices. Section VII presents the experimental validation based on the constructed prototype platform. Finally, Section VIII concludes this article.

II. STRUCTURE AND OPERATIONAL PRINCIPLE OF THE HMW-PD-PWM-CONTROLLED CHB MULTILEVEL INVERTER-BASED MFML-WPT SYSTEM

A System Structure

The MFML-WPT system employing the HMW-PD-PWM-controlled CHB-MLI is shown in Fig. 1.

The MFML-WPT system in Fig. 1 comprises: dc sources ($V_{\mathrm{dc}1}$, $V_{\mathrm{dc}2}$,$\cdots V_{\mathrm{dc}n}$), an n-module cascaded H-bridge multilevel inverter, primary-side multifrequency resonant compensation networks ($C_{\mathrm{p}1}$,$C_{\mathrm{p}2}$,$\cdots$ $C_{\mathrm{p}i}$, $L_{\mathrm{p}1}$,$\cdots L_{\mathrm{p}i}$), transmitting coil with self-inductance (L_{p}), receiving coils with self-inductances ($L_{\mathrm{s}1}$,$L_{\mathrm{s}2}$,$\cdots$ $L_{\mathrm{s}i}$), mutual inductances ($M_{\mathrm{s}1\mathrm{p}}$, $M_{\mathrm{s}2\mathrm{p}}$,$\cdots$ $M_{\mathrm{s}i\mathrm{p}}$), secondary-side compensation capacitors ($C_{\mathrm{s}1}$, $C_{\mathrm{s}2}$,$\cdots$ $C_{\mathrm{s}i}$), notch filters with inductors ($L_{\mathrm{s}1\mathrm{t}1}$,$L_{\mathrm{s}2\mathrm{t}1}$,$\cdots L_{\mathrm{s}i\mathrm{t}i}$), and capacitors ($C_{\mathrm{s}1\mathrm{t}1}$,$C_{\mathrm{s}2\mathrm{t}1}$,$\cdots C_{\mathrm{s}i\mathrm{t}i}$), loads ($R_{\mathrm{L}1}$,$R_{\mathrm{L}2}$,$\cdots$ $R_{\mathrm{L}i}$) and HMW-PD-PWM controller.

B System Operational Principle

As shown in Fig. 1, the HMW-PD-PWM-controlled CHB-MLI-based MFML-WPT system generates multilevel voltage outputs through the superposition of each H-bridge's output voltages. The number of output voltage levels N is

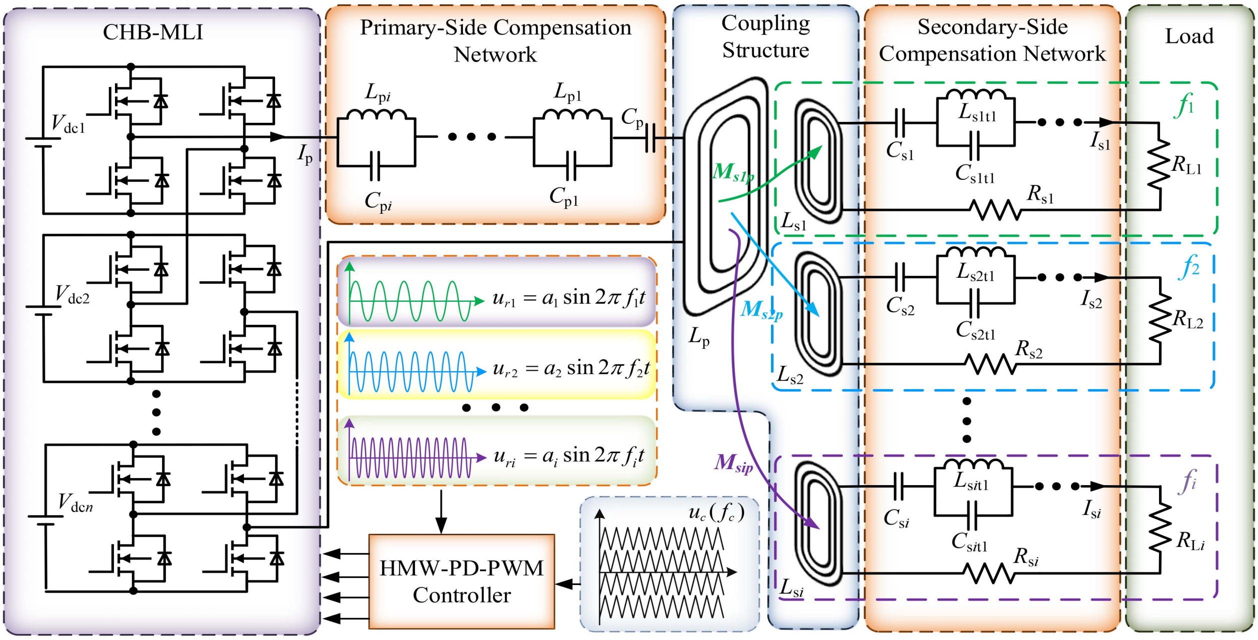

Fig. 1. Configuration of the CHB-MLI-based MFML-WPT system by HMW-PD-PWM.

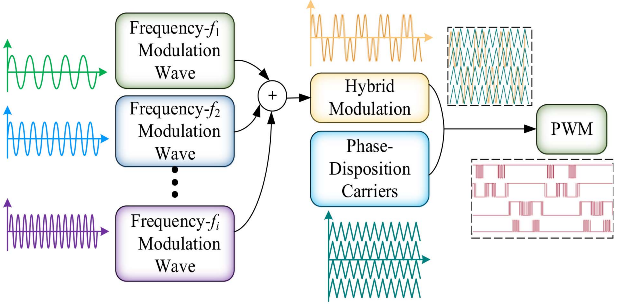

Fig. 2. Operational principle of the HMW-PD-PWM multifrequency modulation scheme.

determined by

$$N = 2n + 1. \tag{1}$$

Although an increase in n leads to a greater number of switching devices, it correspondingly increases the number of output voltage levels produced by the inverter, thereby reducing the harmonic content of the output voltage. Furthermore, by controlling the number of activated H-bridge units, the overall maximum output power of the system can be regulated to meet the demands of multifrequency, high-power loads.

To achieve both multifrequency output and optimal harmonic performance, this article proposes the HMW-PD-PWM multifrequency modulation scheme, as depicted in Fig. 2.

As illustrated in Fig. 2, the resonant frequencies f_1,f_2, …,f_i are determined based on the specific load requirements, while the corresponding modulating wave amplitudes (a_1, a_2, …, a_i) for each resonant frequency are assigned according to the individual load power requirements. These frequency-specific modulating waves are then superimposed, as formulated in

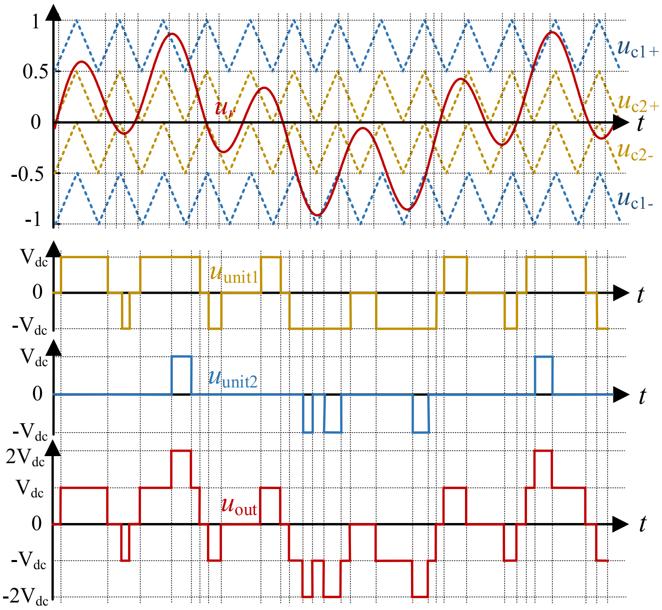

Fig. 3. Implementation process of five-level multifrequency hybrid output.

$$\begin{aligned} u_r &= u_{r1} + u_{r2} + \cdots + u_{rn} \\ &= a_1 \sin(2\pi f_1 t + \theta_1) + a_2 \sin(2\pi f_2 t + \theta_2) + \\ &\quad \cdots a_i \sin(2\pi f_i t + \theta_i). \end{aligned} \tag{2}$$

The specific implementation process of the five-level converter is demonstrated in Fig. 3.

The composite modulating wave u_r is compared with four-layer in-phase carriers. Specifically, the PWM signals generated by the carrier pair $u_{\mathrm{c1+}}$ and $u_{\mathrm{c1-}}$ control the upper H-bridge output voltage u_{unit1}, while those produced by the corresponding carriers $u_{\mathrm{c2+}}$ and $u_{\mathrm{c2-}}$ regulate the lower H-bridge output voltage u_{unit2}. Through voltage superposition, the CHB multilevel inverter achieves multifrequency voltage u_{out} output.

To compensate for reactive power in the system and enhance power factor, this article adopts a MFRC network on the primary side, as illustrated in Fig. 1. This augmented compensation structure integrates multiple parallel *LC* branches in series with the fundamental compensation circuit, thereby increasing the network order to achieve multifrequency resonance. Simultaneously, a notch filter is implemented on the secondary side to suppress cross-coupling and interfrequency interference.

The aforementioned HMW-PD-PWM multifrequency modulation scheme exhibits the following advantages in MFML-WPT systems.

1) The adoption of a CHB-MLI structure significantly mitigates low-order harmonic interference in the receiving circuit and EMI issues caused by high-order harmonics. Furthermore, its inherent modular architecture enables seamless scalability for higher power transmission capacity.
2) By increasing the number of modulating waves and adjusting their frequencies, this methodology enables superimposed power output with arbitrary quantity and frequency combinations, thereby significantly enhancing the compatibility of MFML-WPT systems.
3) By adaptively adjusting the amplitudes of corresponding modulating waves according to individual load power requirements, the output power of loads in different resonant frequency branches can be independently controlled without introducing cross-interference to power delivery in other receiving branches. This amplitude-frequency decoupling strategy significantly enhances the controllability of MFML-WPT systems.
4) Compared to traditional multifrequency multiload WPT systems based on multiinverter superposition, the proposed scheme eliminates issues related to complex cross mutual inductance and associated reactive power compensation challenges. Furthermore, it offers superior economic efficiency, as the number of components does not increase with the number of loads.

III. SYSTEM MODEL OF MFML-WPT UNDER HMW-PD-PWM CONTROL

A System Model

This section develops a system model for the MFML-WPT system under HMW-PD-PWM control, taking a five-level dual-frequency and dual-load configuration with two cascaded H-bridges as a case study. Following the system architecture shown in Fig. 1, the equivalent circuit model is established, as depicted in Fig. 4.

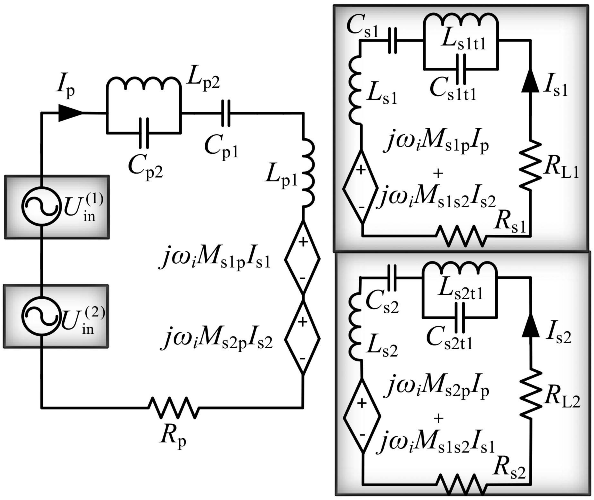

Fig. 4. Equivalent circuit model of the dual-frequency dual-load system.

The analytical approach decomposes the multifrequency power output from the inverter into a superposition of individual frequency components. The voltages ${U_{\mathrm{in}}}^{(1)}$,${U_{\mathrm{in}}}^{(2)}$, corresponding to the resonant frequencies of Channel 1 and Channel 2, respectively, are explicitly expressed, as given in

$$U_{\mathrm{in}}^{(i)} = \frac{a_i \cdot V_{\mathrm{dc}}}{\sqrt{2}}. \tag{3}$$

The system dynamics are governed by Kirchhoff's voltage law equations formulated for both the primary and secondary side networks, as mathematically represented in

$$\begin{cases} U_{\mathrm{in}}^{(i)} = Z_{\mathrm{p}}^{(i)} I_{\mathrm{p}}^{(i)} + j\omega_i M_{\mathrm{s1p}} I_{\mathrm{s1}}^{(i)} + j\omega_i M_{\mathrm{s2p}} I_{\mathrm{s2}}^{(i)} \\ 0 = Z_{\mathrm{s1}}^{(i)} I_{\mathrm{s1}}^{(i)} + j\omega_i M_{\mathrm{s1p}} I_{\mathrm{p}}^{(i)} + j\omega_i M_{\mathrm{s1s2}} I_{\mathrm{s2}}^{(i)} \\ 0 = Z_{\mathrm{s2}}^{(i)} I_{\mathrm{s2}}^{(i)} + j\omega_i M_{\mathrm{s2p}} I_{\mathrm{p}}^{(i)} + j\omega_i M_{\mathrm{s1s2}} I_{\mathrm{s1}}^{(i)}. \end{cases} \tag{4}$$

In (4), the terms ${Z_{\mathrm{p}}}^{(i)}$, ${Z_{\mathrm{s1}}}^{(i)}$, and ${Z_{\mathrm{s2}}}^{(i)}$, denote the input impedances of the primary side and secondary side at distinct frequencies, as explicitly defined in

$$\begin{cases} Z_{\mathrm{p}}^{(i)} = \frac{j\omega_i L_{\mathrm{p2}}}{1-\omega_i^2 L_{\mathrm{p2}} C_{\mathrm{p2}}} + \frac{1}{j\omega_i C_{\mathrm{p1}}} + j\omega_i L_{\mathrm{p1}} + R_{\mathrm{p}} \\ Z_{\mathrm{s1}}^{(i)} = \frac{1}{j\omega_i C_{\mathrm{s1}}} + j\omega_i L_{\mathrm{s1}} + \frac{j\omega_i L_{\mathrm{s1t1}}}{1-\omega_i^2 L_{\mathrm{s1t1}} C_{\mathrm{s1t1}}} + R_{\mathrm{s1}} + R_{\mathrm{L1}} \\ Z_{\mathrm{s2}}^{(i)} = \frac{1}{j\omega_i C_{\mathrm{s2}}} + j\omega_i L_{\mathrm{s2}} + \frac{j\omega_i L_{\mathrm{s2t1}}}{1-\omega_i^2 L_{\mathrm{s2t1}} C_{\mathrm{s2t1}}} + R_{\mathrm{s2}} + R_{\mathrm{L2}} \end{cases} \tag{5}$$

where

$$\omega_i = 2\pi f_i. \tag{6}$$

B Efficiency Analysis

By rearranging (4), the current expressions in the transmitting circuit and individual receiving circuits are derived as presented in

$$\begin{cases} I_{\mathrm{s1}}^{(i)} = -\left(\frac{j\omega_i M_{\mathrm{s1p}} Z_{\mathrm{s2}}^{(i)} + {\omega_i}^2 M_{\mathrm{s1s2}} M_{\mathrm{s2p}}}{Z_{\mathrm{s1}}^{(i)} Z_{\mathrm{s2}}^{(i)} + {\omega_i}^2 M_{\mathrm{s1s2}}^2}\right) \cdot I_{\mathrm{p}}^{(i)} \\ I_{\mathrm{s2}}^{(i)} = -\left(\frac{j\omega_i M_{\mathrm{s2p}} Z_{\mathrm{s1}}^{(i)} + {\omega_i}^2 M_{\mathrm{s1s2}} M_{\mathrm{s1p}}}{Z_{\mathrm{s1}}^{(i)} Z_{\mathrm{s2}}^{(i)} + {\omega_i}^2 M_{\mathrm{s1s2}}^2}\right) \cdot I_{\mathrm{p}}^{(i)} \\ I_{\mathrm{p}}^{(i)} = U_{\mathrm{in}}^{(i)} / (Z_{\mathrm{p}}^{(i)} + ({\omega_i}^2 M_{\mathrm{s1p}}^2 Z_{\mathrm{s2}}^{(i)} + {\omega_i}^2 M_{\mathrm{s2p}}^2 Z_{\mathrm{s1}}^{(i)} - \\ \qquad j2\omega_i^3 M_{\mathrm{s1p}} M_{\mathrm{s2p}} M_{\mathrm{s1s2}}) / Z_{\mathrm{s1}}^{(i)} Z_{\mathrm{s2}}^{(i)} + (\omega_i M_{\mathrm{s1s2}})^2). \end{cases} \tag{7}$$

Consequently, the output power in Channels 1 and 2 can be calculated, as shown in

$$\begin{aligned} P_{\mathrm{o1}}^{(i)} &= \left|I_{\mathrm{s1}}^{(i)}\right|^2 \cdot R_{\mathrm{L1}} \\ &= (U_{\mathrm{in}}^{(i)}(j\omega_i M_{\mathrm{s1p}} Z_{\mathrm{s2}}^{(i)} + {\omega_i}^2 M_{\mathrm{s1s2}} M_{\mathrm{s2p}})/ \\ &\quad Z_{\mathrm{in}}^{(i)}(Z_{\mathrm{s1}}^{(i)} Z_{\mathrm{s2}}^{(i)} + {\omega_i}^2 M_{\mathrm{s1s2}}^2))^2 \cdot R_{\mathrm{L1}} \end{aligned} \tag{8}$$

$$\begin{aligned} P_{\mathrm{o2}}^{(i)} &= \left|I_{\mathrm{s2}}^{(i)}\right|^2 \cdot R_{\mathrm{L2}} \\ &= (U_{\mathrm{in}}^{(i)}(j\omega_i M_{\mathrm{s2p}} Z_{\mathrm{s1}}^{(i)} + {\omega_i}^2 M_{\mathrm{s1s2}} M_{\mathrm{s1p}})/ \\ &\quad (Z_{\mathrm{in}}^{(i)}(Z_{\mathrm{s1}}^{(i)} Z_{\mathrm{s2}}^{(i)} + {\omega_i}^2 M_{\mathrm{s1s2}}^2)))^2 \cdot R_{\mathrm{L2}}. \end{aligned} \tag{9}$$

Additionally, the system input impedance can be derived based on (5), as shown in

$$\begin{aligned} Z_{\mathrm{in}}^{(i)} &= Z_{\mathrm{p}}^{(i)} + \omega_i^2 M_{\mathrm{s1p}}^2 Z_{\mathrm{s2}}^{(i)} + \omega_i^2 M_{\mathrm{s2p}}^2 Z_{\mathrm{s1}}^{(i)} \\ &\quad - j2\omega_i^3 M_{\mathrm{s1p}} M_{\mathrm{s2p}} M_{\mathrm{s1s2}}/(Z_{\mathrm{s1}}^{(i)} Z_{\mathrm{s2}}^{(i)} + \omega_i^2 M_{\mathrm{s1s2}}^2). \end{aligned} \tag{10}$$

The reactive power in the system primarily originates from the inductors, capacitors, and cross mutual inductance between receiving coils. Thus, the total reactive power can be quantified, as formulated in

$$Q^{(i)} = \left|I_{\mathrm{p}}^{(i)}\right|^2 \mathrm{Im}(Z_{\mathrm{in}}^{(i)}). \tag{11}$$

The system's active power loss is shown in

$$P_{\mathrm{loss}}^{(i)} = \left|I_{\mathrm{p}}^{(i)}\right|^2 R_{\mathrm{p}} + \left|I_{\mathrm{s1}}^{(i)}\right|^2 R_{\mathrm{s1}} + \left|I_{\mathrm{s2}}^{(i)}\right|^2 R_{\mathrm{s2}}. \tag{12}$$

Therefore, the transmission efficiency of the system can be derived, as formulated in

$$\eta = \frac{\sum_{i=1}^{j} (P_{\mathrm{o1}}^{(i)} + P_{\mathrm{o2}}^{(i)})}{\sum_{i=1}^{j} (P_{\mathrm{o1}}^{(i)} + P_{\mathrm{o2}}^{(i)} + P_{\mathrm{loss}}^{(i)})}. \tag{13}$$

Meanwhile, the power factor of the system is expressed, as formulated in

$$PF = \frac{\sum_{i=1}^{j} (P_{\mathrm{o1}}^{(i)} + P_{\mathrm{o2}}^{(i)} + P_{\mathrm{loss}}^{(i)})}{\sqrt{\left(\sum_{i=1}^{j} (P_{\mathrm{o1}}^{(i)} + P_{\mathrm{o2}}^{(i)} + P_{\mathrm{loss}}^{(i)})\right)^2 + \left(\sum_{i=1}^{j} Q^{(i)}\right)^2}}. \tag{14}$$

IV. PARAMETER DESIGN METHODOLOGY FOR MFML-WPT SYSTEMS BASED ON HMW-PD-PWM

The research focus of this article lies in achieving synchronized wireless power transmission for multiple loads with arbitrary frequencies, while enabling independent control of the output power for loads at different frequencies and ensuring mutual non-interference between frequency channels. Since cross-coupling between receiving coils and frequency-selective characteristics of the secondary-side network will affect precise power control and system reactive power compensation, this study designs the primary and secondary network configurations to mitigate the influence of cross-coupling and interfrequency interference on system output power.

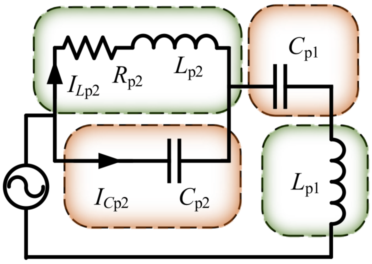

Fig. 5. Configuration of the primary-side resonant compensation network.

A Primary Side Parameter Design

The primary-side MFRC network employed in this work, as illustrated in Fig. 5, simultaneously compensates reactive power generated by multifrequency energy transmission. Furthermore, considering the significant variation of inductor resistance at high operating frequencies, the proposed design methodology explicitly incorporates inductor resistance into the multifrequency resonant network design criteria. Consequently, compared with the approach in [20], this article proposes a simplified yet more accurate parameter design methodology for multifrequency resonant networks.

As observed from Fig. 5, L_{p1} represents the self-inductance of the transmitting coil. Since, its value is generally determined by practical coil design, L_{p1} is treated as a fixed parameter.

Consequently, there remain three unknowns: L_{p2}, C_{p1}, and C_{p2}. The dual-frequency resonant network must operate in resonant states at angular frequencies ω_1 and ω_2, thereby requiring the following relationships among the three parameters to be satisfied:

$$\begin{cases} \frac{\omega_1 L_{\mathrm{p2}}(1-\omega_1^2 C_{\mathrm{p2}} L_{\mathrm{p2}})-\omega_1 C_{\mathrm{p2}} R_{\mathrm{p2}}^2}{(1-\omega_1^2 C_{\mathrm{p2}} L_{\mathrm{p2}})^2+(\omega_1 C_{\mathrm{p2}} R_{\mathrm{p2}})^2} + \omega_1 L_{\mathrm{p1}} - \frac{1}{\omega_1 C_{\mathrm{p1}}} = 0 \\ \frac{\omega_2 L_{\mathrm{p2}}(1-\omega_2^2 C_{\mathrm{p2}} L_{\mathrm{p2}})-\omega_2 C_{\mathrm{p2}} R_{\mathrm{p2}}^2}{(1-\omega_2^2 C_{\mathrm{p2}} L_{\mathrm{p2}})^2+(\omega_2 C_{\mathrm{p2}} R_{\mathrm{p2}})^2} + \omega_2 L_{\mathrm{p1}} - \frac{1}{\omega_2 C_{\mathrm{p1}}} = 0. \end{cases} \tag{15}$$

Since matching capacitance values are more readily adjustable and less prone to variation compared to matching inductance, the compensation inductance L_{p2} is fixed to enable the solvability of (15). This reduces (15) to a system of bivariate functions, allowing the determination of C_{p1} and C_{p2}.

However, this does not imply that all L_{p2} values satisfy practical constraints. As shown in Fig. 5, the parallel configuration of L_{p2} and C_{p2} exhibits a resonant angular frequency ω_n. If ω_n approaches ω_1 or ω_2, the parallel structure will demonstrate extremely high impedance, resulting in excessively high voltage division that may exceed the capacitor's rated voltage. Concurrently, the inductor current risks exceeding its operational limits, potentially causing device failure. Therefore, during the design of L_{p2} and C_{p2}, the following conditions must be considered:

$$\sqrt{\frac{L_{\mathrm{p2}} - C_{\mathrm{p2}} R_{\mathrm{p2}}}{L_{\mathrm{p2}}^2 C_{\mathrm{p2}}}} \notin (\omega_1 - \Delta_1, \omega_1 + \Delta_1) \cup (\omega_2 - \Delta_2, \omega_2 + \Delta_2) \tag{16}$$

where Δ denotes the adjacent frequency range around ω_1 and ω_2. The magnitude of Δ is determined by the voltage withstand

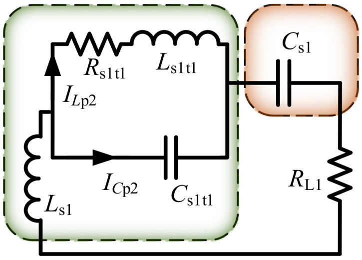

Fig. 6. Configuration of the secondary-side resonant compensation network.

capability and current withstand rating of the capacitors and inductors in practical circuit components.

While the preceding analysis ensures resonant operation at two fixed frequencies, the system compatibility is enhanced to achieve primary-side resonance under arbitrary dual-frequency conditions. This is accomplished by implementing a variable resonant network design referenced from [15], which utilizes switched-capacitor and switched-inductor configurations. Specifically, capacitors C_{p1} and C_{p2} are designed as tunable components, enabling dynamic adjustment of the network's resonant frequencies.

B Secondary Side Parameter Design

Furthermore, the structure of the secondary-side resonant compensation coils is depicted in Fig. 6. This configuration plays a crucial role in mitigating cross-coupling between receiving coils and compensating reactive power on the secondary side.

In contrast to the primary-side resonant network, the secondary-side *LC* parallel network is specifically designed to block interference from other frequency channels on the current channel's output. Consequently, the parameters of the secondary-side *LC* parallel network must satisfy the following constraints:

$$\begin{cases} \omega_2 = \sqrt{\frac{L_{\mathrm{s1t1}} - C_{\mathrm{s1t1}} R_{\mathrm{s1t1}}}{L_{\mathrm{s1t1}}^2 C_{\mathrm{s1t1}}}} \\ \omega_1 = \sqrt{\frac{L_{\mathrm{s2t1}} - C_{\mathrm{s2t1}} R_{\mathrm{s2t1}}}{L_{\mathrm{s2t1}}^2 C_{\mathrm{s2t1}}}}. \end{cases} \tag{17}$$

In the secondary-side circuit, capacitors C_{s1} and C_{s2} are designed to serve the purpose of reactive power compensation. Given that the self-inductances L_{s1} and L_{s2} of the secondary-side coils are predetermined parameters, the values of C_{s1} and C_{s2} must satisfy the following conditions:

$$\begin{aligned} C_{si} = {} & [(1 - \omega_i^2 L_{\mathrm{s}i\mathrm{t1}} C_{\mathrm{s}i\mathrm{t1}})^2 - \omega_i^2 C_{\mathrm{s}i\mathrm{t1}}^2 R_{\mathrm{s}i\mathrm{t1}}^2]/[L_{\mathrm{s}i\mathrm{t1}} \\ & - \omega_i^2 L_{\mathrm{s}i\mathrm{t1}}^2 C_{\mathrm{s}i\mathrm{t1}} - C_{\mathrm{s}i\mathrm{t1}} R_{\mathrm{s}i\mathrm{t1}}^2 + L_{\mathrm{s1}}((1 - \omega_i^2 L_{\mathrm{s}i\mathrm{t1}} C_{\mathrm{s}i\mathrm{t1}})^2 \\ & - \omega_i^2 C_{\mathrm{s}i\mathrm{t1}}^2 R_{\mathrm{s}i\mathrm{t1}}^2)]. \end{aligned} \tag{18}$$

C Multifrequency Parameter Design Procedure

To demonstrate the scalability and effectiveness of the parameter design method presented in this article, we further investigate the system parameter design approach for multifrequency scenarios, assuming N_{load} load frequencies.

The impedances of the *LC* parallel units on the primary side and secondary side are given by (19) and (20), respectively, as follows:

$$Z_j^{(i)} = \frac{\omega_i L_{\mathrm{p}j}(1 - \omega_i^2 C_{\mathrm{p}j} L_{\mathrm{p}j}) - \omega_i C_{\mathrm{p}j} R_{\mathrm{p}j}^2}{(1 - \omega_i^2 C_{\mathrm{p}j} L_{\mathrm{p}j})^2 + (\omega_i C_{\mathrm{p}j} R_{\mathrm{p}j})^2} \tag{19}$$

$$Z_{\mathrm{sit}j}^{(i)} = \frac{\omega_i L_{\mathrm{sit}j}(1 - \omega_i^2 C_{\mathrm{sit}j} L_{\mathrm{sit}j}) - \omega_i C_{\mathrm{sit}j} R_{\mathrm{sit}j}^2}{(1 - \omega_i^2 C_{\mathrm{sit}j} L_{\mathrm{sit}j})^2 + (\omega_i C_{\mathrm{sit}j} R_{\mathrm{sit}j})^2}. \tag{20}$$

Following the approach of first determining the self-inductance of each coil and then solving for the capacitance, the parameters of the primary-side multifrequency resonant network are derived by solving the system of

$$\begin{cases} \sum_{2}^{N_{load}} Z_j^{(1)} + \omega_1 L_{\mathrm{p1}} - 1/\omega_1 C_{\mathrm{p1}} = 0 \\ \sum_{2}^{N_{load}} Z_j^{(2)} + \omega_2 L_{\mathrm{p1}} - 1/\omega_2 C_{\mathrm{p1}} = 0 \\ \qquad \cdots \\ \sum_{2}^{N_{load}} Z_j^{(i)} + \omega_i L_{\mathrm{p1}} - 1/\omega_i C_{\mathrm{p1}} = 0. \end{cases} \tag{21}$$

The simultaneous solution must satisfy the following constraints:

$$Z_j^{(i)} \ll \infty. \tag{22}$$

If the system of equations yields no solution, the inductance parameters must be redefined, and through iterative recalculation, compliant capacitance values can be determined.

For the secondary-side parameter design in multifrequency systems, the capacitance values for the notch filter $Z_{sitj}{}^{(i)}$are determined based on the known secondary resonant frequencies, followed by calculating the resonant capacitance $C_{\mathrm{s}i}$ using

$$\sum_{j=1}^{N_{load}-1} Z_{\mathrm{sit}j}^{(i)} + \omega_i L_{\mathrm{s}i} - 1/\omega_i C_{\mathrm{s}i} = 0. \tag{23}$$

Similarly, if the equations yield no solution, the inductance parameters must be redefined, and an iterative refinement loop is executed. Based on the methodology above, a multifrequency parameter design flowchart has been developed, as illustrated in Fig. 7.

V. PERFORMANCE ANALYSIS OF THE HMW-PD-PWM-CONTROLLED MFML-WPT SYSTEM

The MFML-WPT system should demonstrate excellent cross-coupling suppression, interfrequency interference rejection, and independent power regulation capabilities among multiple loads. Additionally, the energy efficiency characteristics of the system require thorough analysis.

A. Cross-Coupling Suppression Characteristics

As analytically derived from (8), (9), and (14), the cross mutual inductance M_{s1s2} between receiving coils introduces adverse impacts on the output power of individual frequency transmission channels while increasing the system's reactive power.

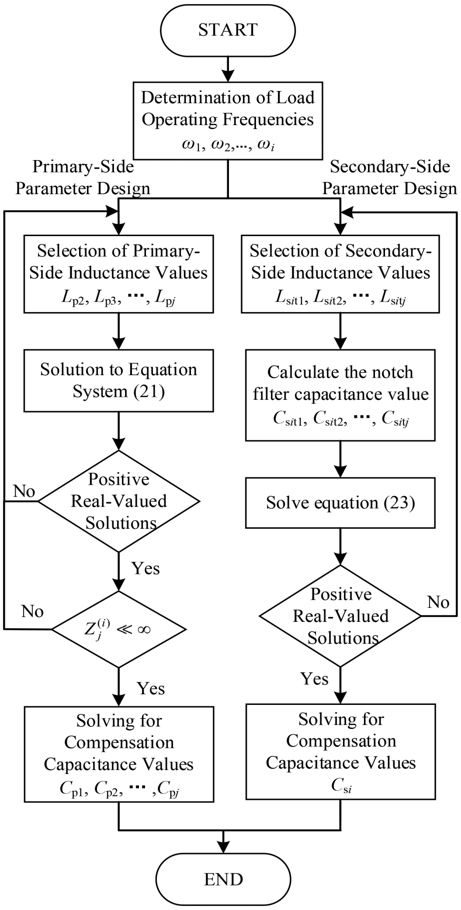

Fig. 7. Parameter design workflow for primary/secondary-side resonant networks in multifrequency systems.

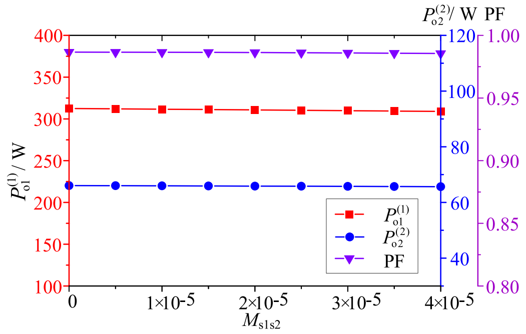

Fig. 8. Output power and power factor characteristics versus M_{s1s2} variation.

To address this challenge, notch filters are strategically implemented in the secondary circuits to suppress cross-coupling effects. Leveraging the established system model and parameters detailed in Section III, the dynamic influence of M_{s1s2} variation on both output power distribution and power factor characteristics is systematically investigated, with quantitative results presented in Fig. 8.

As evidenced in Fig. 8, the output power of both transmission channels remains virtually unaffected with increasing cross mutual inductance M_{s1s2}, demonstrating the system's capability to effectively suppress cross-coupling interference in independent power regulation. Simultaneously, the system power factor exhibits negligible variation under M_{s1s2} perturbation, indicating that the reactive power remains stable despite mutual coupling fluctuations. These analytical results conclusively validate the proposed system's robust cross-coupling suppression characteristics.

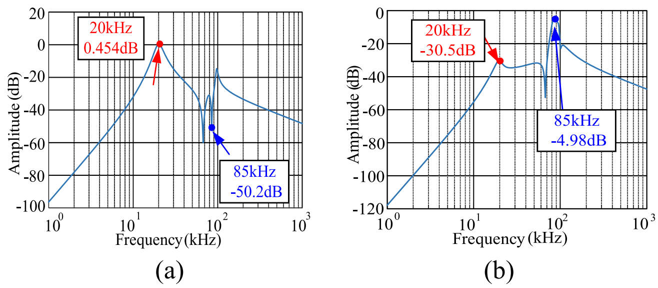

Fig. 9. Dual-channel magnitude-frequency response characteristics. (a) 20 kHz. (b) 85 kHz.

B Cross-Frequency Interference Suppression Characteristics

To characterize the system's interfrequency interference rejection performance, this work analyzes the frequency-selective characteristics of individual channels by deriving the transfer functions $G_1(s)$ and $G_2(s)$, defined in (24) and (25), respectively. These transfer functions are calculated as the ratio of each channel's output voltage to the system's input voltage

$$\begin{aligned} G_1(s) &= \frac{U_{o1}^{(i)}(s)}{U_{in}^{(i)}(s)} \\ &= -\frac{sM_{s1p}Z_{s2}(s) - s^2M_{s1s2}M_{s2p}}{Z_{s1}(s)Z_{s2}(s) - s^2M_{s1s2}^2} \cdot R_{L1} \Bigg/ \Bigg(Z_p(s) \\ &\quad - sM_{s1p} \cdot \frac{sM_{s1p}Z_{s2}(s) - s^2M_{s1s2}M_{s2p}}{Z_{s1}(s)Z_{s2}(s) - s^2M_{s1s2}^2} \\ &\quad - sM_{s2p} \cdot \frac{sM_{s2p}Z_{s1}(s) - s^2M_{s1s2}M_{s1p}}{Z_{s1}(s)Z_{s2}(s) - s^2M_{s1s2}^2} \Bigg) \end{aligned} \tag{24}$$

$$\begin{aligned} G_2(s) &= \frac{U_{o2}^{(i)}(s)}{U_{in}^{(i)}(s)} \\ &= -\frac{sM_{s1p}Z_{s2}(s) - s^2M_{s1s2}M_{s2p}}{Z_{s1}(s)Z_{s2}(s) - s^2M_{s1s2}^2} \cdot R_{L2} \Bigg/ \Bigg(Z_{\mathrm{p}}(s) \\ &\quad - sM_{s1p} \cdot \frac{sM_{s1p}Z_{s2}(s) - s^2M_{s1s2}M_{s2p}}{Z_{s1}(s)Z_{s2}(s) - s^2M_{s1s2}^2} \\ &\quad - sM_{s2p} \cdot \frac{sM_{s2p}Z_{s1}(s) - s^2M_{s1s2}M_{s1p}}{Z_{s1}(s)Z_{s2}(s) - s^2M_{s1s2}^2} \Bigg). \end{aligned} \tag{25}$$

Fig. 9 magnitude-frequency response characteristics of 20 kHz and 85 kHz transmission channels.

As demonstrated in Fig. 9(a), the 20 kHz resonant channel exhibits a voltage gain of 0.454 dB relative to the 20 kHz

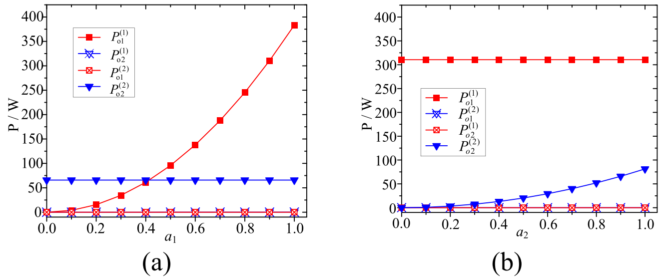

Fig. 10. Output power versus modulating amplitude (a_i) variation characteristics. (a) a_1. (b) a_2.

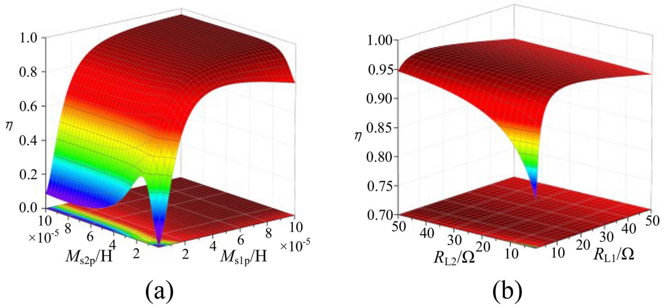

Fig. 11. System power transfer efficiency surface characteristics versus mutual inductance and load variations. (a) Mutual inductance. (b) Load.

voltage component of the CHB output. Conversely, the 20 kHz resonant channel achieves −50.2 dB gain against the 85 kHz voltage component from the CHB output, confirming its effective suppression of 85 kHz energy. Similarly, Fig. 9(b) indicates that the 85 kHz resonant channel attains −30.5 dB gain for the 20 kHz CHB output component and −4.98 dB gain for its native 85 kHz component. These results demonstrate superior suppression effectiveness of the 85 kHz resonant channel against 20 kHz interference. Consequently, the proposed system exhibits excellent interfrequency interference suppression capabilities.

C Independent Power Regulation Characteristics

As proposed in Section II, the output power of individual frequency channels in the HMW-PD-PWM scheme can be independently regulated by controlling the amplitudes a_1 and a_2 of their corresponding modulating waveforms. The relationship between the output power of each frequency channel and the modulating wave amplitudes is governed by

$$\begin{cases} P_{\mathrm{o1}}^{(i)} = \left(\dfrac{V_{\mathrm{dc}}(j\omega_i M_{\mathrm{s1p}} Z_{\mathrm{s2}}^{(i)} + {\omega_i}^2 M_{\mathrm{s1s2}} M_{\mathrm{s2p}})}{\sqrt{2} Z_{\mathrm{in}}^{(i)} (Z_{\mathrm{s1}}^{(i)} Z_{\mathrm{s2}}^{(i)} + {\omega_i}^2 M_{\mathrm{s1s2}}^2)} \right)^2 \cdot R_{\mathrm{L1}} \cdot a_i^2 \\ P_{\mathrm{o2}}^{(i)} = \left(\dfrac{V_{\mathrm{dc}}(j\omega_i M_{\mathrm{s2p}} Z_{\mathrm{s1}}^{(i)} + {\omega_i}^2 M_{\mathrm{s1s2}} M_{\mathrm{s1p}})}{\sqrt{2} Z_{\mathrm{in}}^{(i)} (Z_{\mathrm{s1}}^{(i)} Z_{\mathrm{s2}}^{(i)} + {\omega_i}^2 M_{\mathrm{s1s2}}^2)} \right)^2 \cdot R_{\mathrm{L2}} \cdot a_i^2. \end{cases} \tag{26}$$

As indicated by (26), the output power of each channel is related to a_1 and a_2. Calculations under varying a_i values reveal the output power characteristics of individual channels, as demonstrated in Fig. 10.

As observed from Fig. 10(a), when the modulating amplitude a_2 corresponding to 85 kHz remains constant, the output power ${P_{\mathrm{o1}}}^{(1)}$ of the 20 kHz channel increases proportionally as a_1 varies from 0 to 1, while ${P_{\mathrm{o2}}}^{(2)}$ remains essentially unchanged. Similarly, Fig. 10(b) demonstrates that adjusting a_2 exclusively induces a corresponding increase in ${P_{\mathrm{o2}}}^{(2)}$, whereas ${P_{\mathrm{o1}}}^{(1)}$ maintains stable operation. These results conclusively validate that the proposed system achieves precise independent control of output power by solely modifying the modulating amplitude of the corresponding frequency channel, without mutual interference.

D System Power Transfer Efficiency

Based on (8), (9), and (13), this study analyzes the power transfer efficiency characteristics of the system under load and mutual inductance variations during operation. The trend of overall system efficiency versus load and mutual inductance variations is demonstrated in Fig. 11.

As shown in Fig. 11(a), the system maintains high power transfer efficiency η across a wide range of mutual inductance variations. The efficiency η is significantly influenced by M_{s1p}, thus, M_{s1p} should not be excessively small to ensure high efficiency. Additionally, Fig. 11(b) indicates that the system efficiency is minimally affected by load variations, i.e., even when the impedances R_{L1} and R_{L2} vary during wireless power transfer, the system consistently sustains high efficiency. Therefore, the proposed system achieves highly efficient operation under mutual inductance and load parameter perturbations.

VI. CHB-MLI BALANCING OPTIMIZATION

A Imbalance Phenomena and Root Cause Analysis

As discussed in the previous section, the power distribution among frequency channels is achieved by adjusting the amplitudes of the modulating waveforms. However, when the superimposed sinusoidal wave amplitude decreases, particularly when the modulation index drops below 0.5, as shown in Fig. 12.

The uppermost carrier $u_{\mathrm{c1+}}$, and the lowermost carrier $u_{\mathrm{c1-}}$ no longer intersect with the composite modulating waveform u_{r}. Under this condition, the upper switches of the upper H-bridge cell remain continuously ON, while the lower switches remain OFF, resulting in zero output voltage from the upper H-bridge cell. Consequently, the total output voltage of the CHB-MLI is solely provided by the lower H-bridge cell.

This leads to imbalanced output power between the upper and lower H-bridge cells, concentrates switching losses predominantly in the lower H-bridge cell, significantly reduces the lifespan of the lower switches, increases fault risks, and degrades system reliability. Additionally, the irregularity of the multifrequency superimposed waveform causes uneven switching losses among the power devices.

When the upper-layer carriers $u_{\mathrm{c1+}}$ and $u_{\mathrm{c1-}}$ do not intersect with the modulating wave, and the modulating wave is entirely contained within the $u_{\mathrm{c2+}}$ and $u_{\mathrm{c2-}}$ carrier layers, the equivalent modulating waves for the upper and lower H-bridge cells are expressed as

$$\begin{cases} u_{\mathrm{rh1}} = 0 \\ u_{\mathrm{rh2}} = a_1 \sin(2\pi f_1 t) + a_2 \sin(2\pi f_2 t) \end{cases}. \tag{27}$$

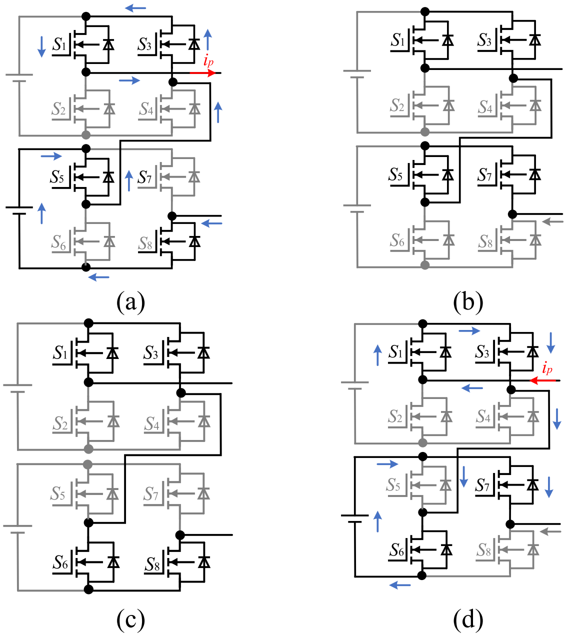

Fig. 12. Conduction states at modulation index below 0.5. (a) Positive voltage output condution mode. (b) No voltage output conduction mode 1. (c) No voltage output conduction mode 2. (d) Negative voltage output conduction mode.

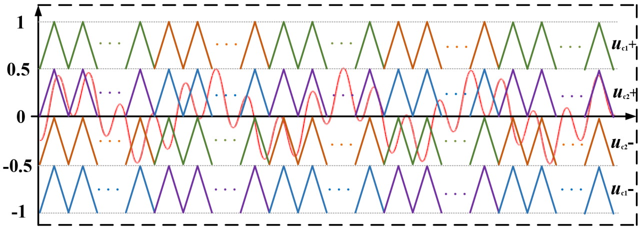

Fig. 13. Carrier reconstruction schematic.

Given the low output harmonic content inherent in multilevel inverters, only the fundamental component of the output voltage is considered. Therefore, the fundamental output voltages of the upper and lower H-bridge cells are expressed as

$$\begin{cases} u_{\mathrm{h1}} = 0 \\ u_{\mathrm{h2}} = m_1 V_{\mathrm{dc}} \sin(2\pi f_1 t) + m_2 V_{\mathrm{dc}} \sin(2\pi f_2 t) \end{cases}. \tag{28}$$

As derived from (28), the upper H-bridge cell exhibits zero power output, resulting in full power transmission through the lower H-bridge cell. This configuration significantly increases operational stress on the lower H-bridge cell, adversely affecting the inverter's long-term operational reliability.

B Carrier Reconstruction-Based Balancing Optimization

To mitigate the adverse effects of power imbalance and loss imbalance on system reliability during the multifrequency modulation process, this article employs a carrier reconstruction method, as illustrated in Fig. 13.

As shown in Fig. 13, the proposed method relocates k cycles of the edge carriers $u_{\mathrm{c1+}}$ and $u_{\mathrm{c1-}}$ to the intermediate carrier layers $u_{\mathrm{c2+}}$ and $u_{\mathrm{c2-}}$, with a k-cycle interval before subsequent relocations. Simultaneously, k cycles from the intermediate layers $u_{\mathrm{c2+}}$ and $u_{\mathrm{c2-}}$ are inserted into the vacant segments of the edge carrier layers $u_{\mathrm{c1+}}$ and $u_{\mathrm{c1-}}$, followed by an m-cycle interval before the next adjustment.

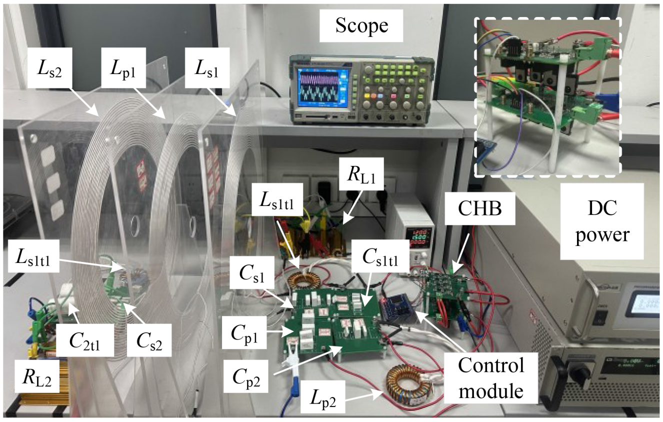

Fig. 14. Dual-frequency dual-load WPT experimental platform for CHB-MLI.

To quantify the system's power balancing performance, the power balancing coefficient S is defined as

$$S = \frac{u_{\mathrm{unit1}}}{u_{\mathrm{unit2}}} = s(\Delta\theta, k) \tag{29}$$

where u_{unit1} and u_{unit2} denote the output voltages of the two H-bridge cells, and $\Delta\theta$ represents the phase difference between the modulating waves of different frequencies.

Through iterative optimization of $\Delta\theta$ and k, the power balancing coefficient S can be driven to approach unity, indicating balanced output power among H-bridge cells and equitable distribution of switching losses.

VII. SIMULATION AND EXPERIMENTAL VERIFICATION

To validate the effectiveness of the proposed HMW-PD-PWM-controlled MFML WPT system, a dual H-bridge cascaded experimental platform for dual-frequency dual-load WPT was constructed, as shown in Fig. 14.

The CHB multilevel inverter employs SiC MOSFETS (C3M0040120D) featuring a 1200 V drain-to-source voltage rating and 66 A continuous drain current. The devices' ultrafast switching capability makes them particularly suitable for high-frequency WPT systems with multiple loads. Switching signals are generated by a TMS320F28335 controller operating at 680 kHz switching frequency, with 80 ns dead time implemented to prevent shoot-through faults. Furthermore, the dc power supplies are galvanically isolated and configured in series to enable proper CHB-MLI operation. The other experimental parameters are shown in Table I.

A. Verification of Multifrequency Output Performance in CHB-MLI

To validate the multifrequency output characteristics of the CHB-MLI, a dual H-bridge cascaded dual-frequency dual-load

TABLE I
DESIGNED PARAMETERS OF THE MFML-WPT SYSTEM

Parameter	**Value**
Resonant Frequencies f_1, f_2	20, 85kHz
Primary Compensation Capacitors C_{p1}, C_{p2}	280.80, 72.70nF
Coil Inductances L_{p1}, L_{s1}, L_{s2}	136.0, 236.7, 233.38μH
Secondary Compensation Capacitors C_{s1}, C_{s2}	192.86, 14.09nF
Mutual Inductances $M_{s1p}, M_{s2p}, M_{s1s2}$	94.2, 64.8, 22.3μH
Primary Compensation Inductance L_{p2}	77.11μH
Loads R_{L1}, R_{L2}	12, 20Ω
Resistances R_{p1}, R_{s1}, R_{s2}	0.18, 0.27, 0.32Ω
Notch Inductors L_{s1t1}, L_{s2t1}	76.18, 21.58μH
Notch Capacitors C_{s1t1}, C_{s2t1}	46.15nF, 2.952μF
Notch Inductor Resistances R_{s1t1}, R_{s2t1}	0.36, 0.11Ω
Transmit-Receive Coil Distances d_{s1p}, d_{s2p}	5, 12cm
Input DC voltage V_{dc1}, V_{dc2}	100, 100V
20kHz channel output power	223.14W
85kHz channel output power	45.13W

WPT system was configured. The CHB-MLI simultaneously generates a five-level voltage output combining 20 kHz and 85 kHz components. The modulating wave amplitudes are set to $a_1 = 0.45$ and $a_2 = 0.45$. The simulated waveforms and corresponding fast Fourier transform (FFT) analysis under the designed parameters are presented in Fig. 15.

As observed in Fig. 15(a), the CHB-MLI under HMW-PD-PWM control achieves multifrequency power delivery, with the output voltage spectrum [see Fig. 15(c)] demonstrating exclusive dominance of 20 kHz and 85 kHz frequency components. The absence of spurious frequency components in the low-frequency spectrum corroborates the experimental voltage and current waveforms in Fig. 15(b), confirming that the proposed HMW-PD-PWM control strategy enables multifrequency power output in CHB-MLI.

The simulated and experimental waveforms of the system load current and their FFT analysis are shown in Fig. 16.

As shown in Fig. 16(a) and (b), the consistency between simulation and measurement is validated. Combined with Fig. 16(c) and (d), the 20 kHz-resonant transmission channel exclusively delivers 20 kHz power components, while the 85 kHz-resonant channel predominantly transmits 85 kHz power. These results demonstrate the system's superior frequency-selective characteristics with negligible interchannel interference, Simultaneously, the figure reveals that harmonics exhibit negligible effects on the secondary-side power output, resulting in minimal harmonic interference. Furthermore, it is experimentally confirmed that high-frequency electromagnetic interference originating from the primary side is effectively isolated from the secondary receiving side through suppression of conductive coupling pathways.

B. System Dynamic Response Verification

To validate the system's dynamic characteristics during power variation and frequency switching processes, this work investigates the transient behavior during mode transitions between single-frequency operation and dual-frequency operation under dual-frequency dual-load conditions, as shown in Fig. 17.

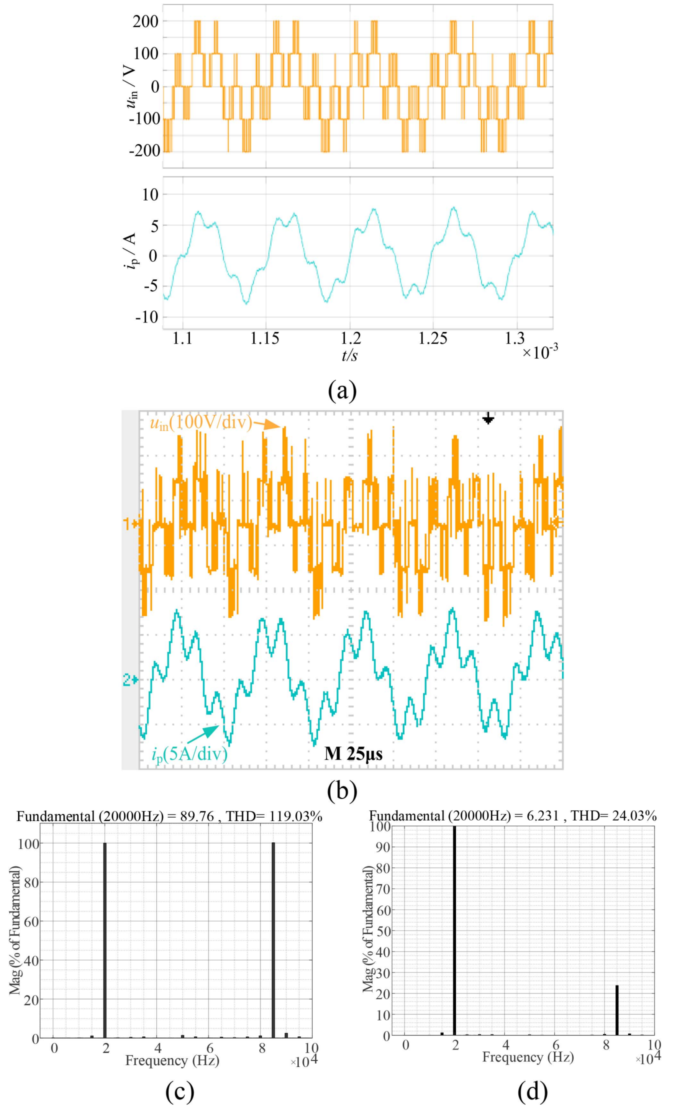

(a)

(b)

(c)

(d)

Fig. 15. Output voltage and current waveforms and FFT analysis of the inverter. (a) Simulated waveforms. (b) Experimental waveforms. (c) Output voltage FFT analysis. (d) Output current FFT analysis.

As shown in Fig. 17, prior to t_1, the modulating wave amplitude corresponding to 85 kHz is $a_1 = 0.45$, while the amplitude for 20 kHz is $a_2 = 0$. Due to the low modulation depth, the inverter output voltage u_{in} degenerates into a three-level waveform and exclusively transmits 85 kHz power components, resulting in the 20 kHz load current i_{s1} approaching zero, thereby operating in 85 kHz single-frequency mode. During t_1 to t_2, both modulating wave amplitudes (a_1 and a_2) for 85 kHz and 20 kHz are set to 0.45. Consequently, the output voltage u_{in} regenerates a five-level waveform, inducing currents in both 85 kHz and 20 kHz loads, confirming dual-frequency operation. After t_2, the 85 kHz amplitude a_1 is disabled ($a_1 = 0$), while the 20 kHz amplitude a_2 remains at 0.45. The output voltage u_{in} reverts to a three-level waveform, transmitting only 20 kHz power components, which reduces the 85 kHz load current i_{s2} to near zero, thus establishing 20 kHz single-frequency operation.

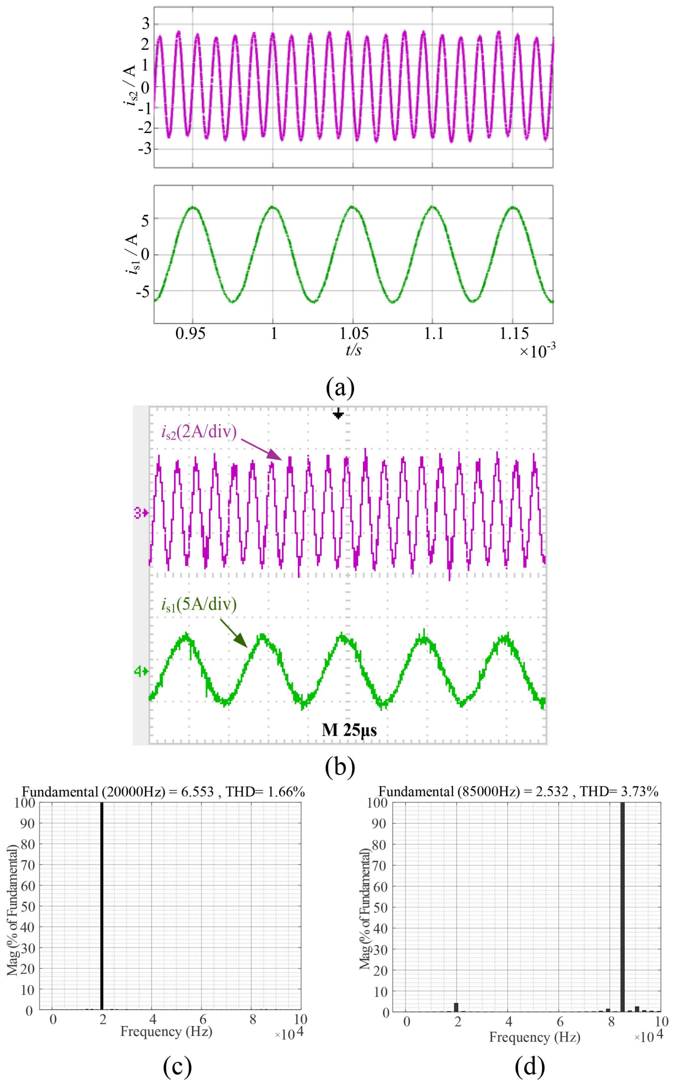

(a)

(b)

(c)

(d)

Fig. 16. Load current waveforms and frequency spectrum analysis. (a) Simulated waveforms. (b) Experimental wave-forms. (c) 20 kHz channel current FFT analysis. (d) 85 kHz channel current FFT analysis.

Additionally, the output power of the system under different modulation indices were compared, as shown in Fig. 18.

From Fig. 18, it can be observed that the power exhibits a similar trend in variation for both experimental and simulation results. Dynamically adjusting the amplitude of the modulating wave allows for dynamic control of the output power, enabling full-range power adjustment. The discrepancy between the measured and simulated values is primarily attributed to inverter losses.

Meanwhile, to evaluate the anti-interference performance of the system under dynamic variations in mutual inductance, the range of mutual inductance changes was determined based on measurements taken under a 4 cm horizontal misalignment and a vertical misalignment variation of ±1 cm in the magnetic coupler structure. Within this range, tests were conducted to assess the system's output power performance. The corresponding results are presented in Fig. 19.

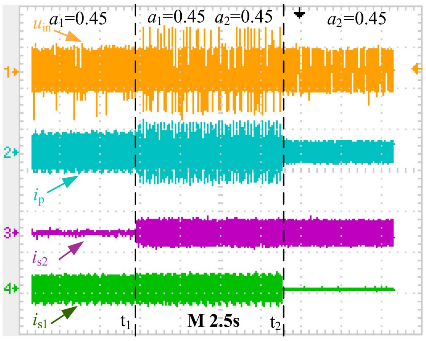

Fig. 17. Experimental results of single-frequency and dual-frequency mode transitions.

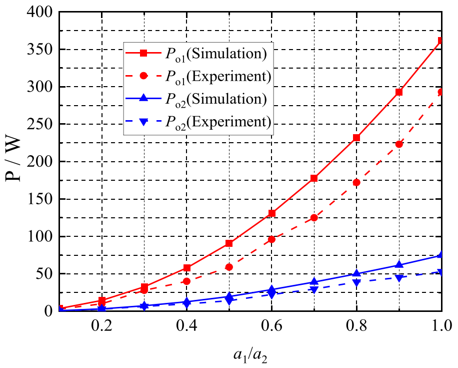

Fig. 18. Measured and simulated output power of the system under different modulation indices.

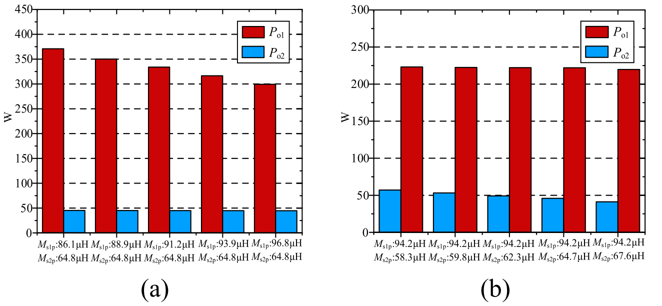

(a)

(b)

Fig. 19. Output Power under coil misalignment. (a) During Variation of M_{s1p}. (b) During variation of M_{s2p}.

As can be observed from Fig. 19, It can be observed that when the mutual inductance M_{s1p} varies, it primarily affects the output power P_{o1} of Channel 1, while having almost no influence on the output power P_{o2} of Channel 2. Similarly, a change in the mutual inductance M_{s2p} influences P_{o2} without significantly affecting P_{o1}. This indicates that the two channels exhibit strong decoupling characteristics and operate without mutual interference.

The experimental results of multimode transitions validate two critical aspects: 1) the proposed HMW-PD-PWM multi-frequency modulation strategy enables continuous power and frequency regulation capability through dynamic carrier reconstruction and 2) the system exhibits superior anti-interference characteristics against cross-frequency components, providing

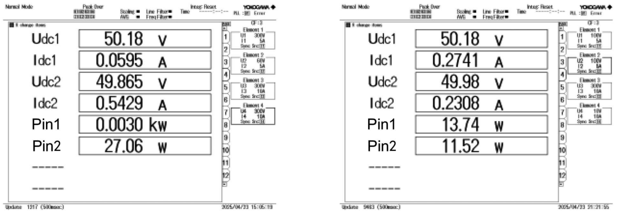
Udc1 50.18 V
Idc1 0.0595 A
Udc2 49.865 V
Idc2 0.5429 A
Pin1 0.0030 kW
Pin2 27.06 W

(a)

Udc1 50.18 V
Idc1 0.2741 A
Udc2 49.98 V
Idc2 0.2308 A
Pin1 13.74 W
Pin2 11.52 W

(b)

Fig. 20. H-bridge input power analysis before and after optimization. (a) Before optimization. (b) After optimization.

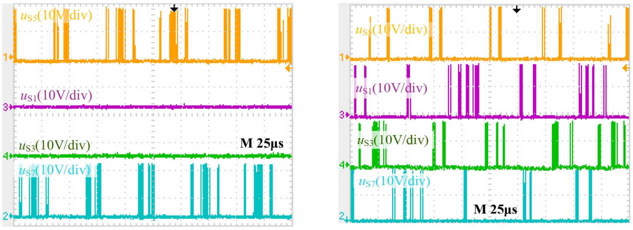

(a) (b)

Fig. 21. Inverter gate drive voltage waveforms before and after optimization. (a) Before optimization. (b) After optimization.

essential conditions for achieving precision power control in multiload wireless power transfer applications.

C Power and Loss Balancing Verification

To validate the power and loss balancing performance among H-bridge cells enabled by the proposed carrier reconstruction method, this study configures both 20 kHz and 85 kHz modulating wave amplitudes at $a_1 = a_2 = 0.2$. The power distribution before and after optimization is depicted in Fig. 20, where $P_{\text{in}1}$ and $P_{\text{in}2}$ denote the input power of the upper and lower H-bridge cells, respectively.

As shown in Fig. 20(a), without balancing optimization, the upper H-bridge cell exhibits negligible input power, while the output power is predominantly concentrated in the lower H-bridge cell, indicating extremely imbalanced power distribution. After applying the balancing optimization [see Fig. 20(b)], under dual-frequency modulation, the input power ratios of the upper and lower H-bridge cells reach 54.4% and 45.6%, respectively, significantly mitigating the power imbalance issue.

Furthermore, the switching loss distribution among H-bridge cells can be characterized by the switching counts per switching period. The gate drive voltage patterns before and after balancing optimization are depicted in Fig. 21. Since the two switches in each bridge leg operate with complementary gate drive voltages, the figure exclusively illustrates the upper switch drive voltages of each bridge leg.

As shown in Fig. 21, before optimization, switches S_1 and S_3 remain in a constantly closed state, while S_2 and S_4 also maintain an open state, resulting in concentrated switching actions in the lower H-bridge unit (S_5–S_8). After optimization, the switching counts of the upper H-bridge switches S_1–S_4 increase, whereas the switching frequency of the lower H-bridge switches S_5–S_8 decreases proportionally. This demonstrates that the proposed balancing optimization effectively achieves switching loss equalization across H-bridge cells.

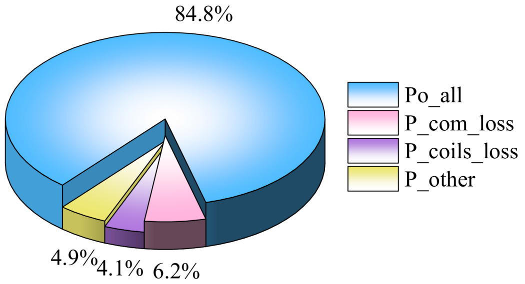

Fig. 22. System active power analysis.

D System Efficiency and Power Factor

System efficiency was analyzed through experimental measurements and calculations on a 300 W output system, with the power distribution within the system illustrated in Fig. 22.

The total active power in the system is primarily composed of the total output power $P_{\text{o\_all}}$, active power losses in the primary and secondary coils ($P_{\text{coils\_loss}}$), compensation network losses ($P_{\text{com\_loss}}$), and other active power losses (P_{other}). As shown in Fig. 19, the system achieves an overall efficiency of 84.8%. Due to the high-frequency operation and the presence of multiple magnetic components in the compensation network, which exhibit higher internal resistance, the active power losses in the compensation network significantly impact the total system efficiency.

As demonstrated by comparing the phase relationship between the inverter output voltage and current in Fig. 15, the system's power factor remains elevated after implementing the multifrequency resonant network, Therefore, the proposed scheme demonstrates a superior reactive power compensation method, as compared to the traditional multinverter approach, without the need to consider the effects of cross mutual inductance.

E Comparison With Previous Work

To demonstrate the advantages of the proposed CHB-MLI based on MFML-WPT system presented in this article, Table II summarizes a performance comparison between the proposed system and prior work.

As shown in Table II, the comparison focuses on key performance aspects including online regulation capability, independent power control, output power, power factor, and efficiency. Significant cross-coupling between receiving coils in [6] prevents independent power control across frequency channels, while the uncompensated reactive power results in a low system power factor. The system in [8], utilizing odd-order harmonics for power transfer, exhibits difficulties in output power control. The time-division multiplexing approach adopted in [10] precludes simultaneous power delivery and suffers from low transmission efficiency. Lack of reactive power compensation in [14] leads to a low power factor, and the solution in [16] is suitable only for low-power applications, rendering it inadequate

TABLE II
COMPARISON OF DIFFERENT MFML-WPT TECHNOLOGIES

	Transmission Principle	Online Adjustment	Independent Power Control	Power Factor	Output Power	η(%)
[6]	Parallel operation of multiple inverters	Yes	No	low	180 w	73–80
[8]	Fundamental and harmonic components	No	No	low	40 w	64.74
[10]	Time-sharing	Yes	Yes	high	2 w	24–29
[14]	HMW-PWM	Yes	Yes	low	40 w	65–70
[16]	HC Control	Yes	Yes	high	15 w	80–90
Proposed	HMW-PD-PWM	Yes	Yes	high	300 W	84.8

for high-power demands with multiple loads. In contrast, the MFML-WPT system with HMW-PD-PWM control proposed in this article enables continuous and independent regulation of output power across all frequency channels while maintaining high efficiency and power factor, making it well-suited for high-power scenarios involving multiple loads.

VIII. CONCLUSION

This article proposes an MFML-WPT system based on CHB-MLI, along with the HMW-PD-PWM multifrequency modulation methodology. First, the system architecture and operational principles are introduced, where multifrequency power delivery is achieved through a codirectional carrier disposition method with superimposed modulating waves. Subsequently, a five-level dual-frequency and dual-load configuration is established as a case study, followed by equivalent circuit modeling. The primaryside and secondside parameters are systematically designed, with thorough analysis of cross-coupling suppression and inter-frequency interference mitigation characteristics. Furthermore, the inherent power imbalance and loss imbalance among H-bridge cells under low modulation indices are investigated, addressed through an optimized carrier reconstruction strategy to enhance power distribution uniformity. Experimental validation confirms the effectiveness of the proposed approach.

Experimental results demonstrate that the proposed CHB-MLI enables multifrequency power output with continuous adjustment of output frequency and power, exhibiting excellent compatibility. The system shows minimal interference between receiving channels and strong anti-interference capability, This offers a novel solution for multifrequency, cluster-based high-power wireless power transfer scenarios, such as simultaneous charging of electric vehicles with varying power and frequency requirements.

However, the proposed system still has some shortcomings, which warrant further research in the following aspects.

1) To achieve the power quality associated with multilevel voltage output, the HMW-PD-PWM method employs a higher carrier frequency, resulting in significant system switching losses. Further research is needed to reduce system switching losses and achieve soft-switching operation.
2) The present study has not yet investigated control strategies for maintaining stable system output under variations in mutual inductance caused by magnetic coupler misalignment or changes in load conditions. In subsequent work, we will focus on developing control schemes capable of achieving constant-current and constant-voltage output for each channel within the proposed system.

REFERENCES

[1] A. Sagar et al., “A comprehensive review of the recent development of wireless power transfer technologies for electric vehicle charging systems,” *IEEE Access*, vol. 11, pp. 83703–83751, 2023.

[2] C. Z. Hang et al., “A strong misalignment-tolerance wireless power transfer system based on dynamic diffusion magnetic field for unmanned aerial vehicle applications,” *IEEE Trans. Power Electron.*, vol. 39, no. 11, pp. 14129–14134, Nov. 2024.

[3] C. Cai, J. Li, S. Wu, Z. Qin, W. CHai, and S. Yang, “A bipolar and unipolar magnetic channel multiplexed WPT system with simultaneous full-duplex communication for autonomous underwater vehicles,” *IEEE Trans. Power Electron.*, vol. 38, no. 12, pp. 15086–15090, Dec. 2023.

[4] X. Wang, S. SHa, J. He, L. Guo, and M. Lu, “Wireless power delivery to low-power mobile devices based on retro-reflective beamforming,” *IEEE Antennas Wireless Propag. Lett.*, vol. 13, pp. 919–922, 2014.

[5] Z. Nie and Y. Yang, “A model independent scheme of adaptive focusing for wireless powering to in-body shifting medical device,” *IEEE Trans. Antennas Propag.*, vol. 66, no. 3, pp. 1497–1506, Mar. 2018.

[6] F. Liu, Y. Yang, Z. Ding, X. Chen, and R. M. Kennel, “A multifrequency superposition methodology to achieve high efficiency and targeted power distribution for a multiload MCR WPT system,” *IEEE Trans. Power Electron.*, vol. 33, no. 10, pp. 9005–9016, Oct. 2018.

[7] D. AHn and P. P. Mercier, “Wireless power transfer with concurrent 200-kHz and 6.78-MHz operation in a single-transmitter device,” *IEEE Trans. Power Electron.*, vol. 31, no. 7, pp. 5018–5029, Jul. 2016.

[8] W. Liu, K. T. CHau, C. H. T. Lee, C. Jiang, W. Han, and W. H. Lam, “Multi-frequency multi-power one-to-many wireless power transfer system,” *IEEE Trans. Magn.*, vol. 55, no. 7, Jul. 2019, Art. no. 8001609.

[9] C. Wang, F. Li, and Y. Cao, “Dual-frequency dual-type-output wireless power transfer system with independent adjustable outputs,” *IEEE J. Emerg. Sel. Topics Power Electron.*, vol. 13, no. 4, pp. 4301–4314, Aug. 2025.

[10] Y.-J. Kim, D. Ha, W. J. Chappell, and P. P. Irazoqui, “Selective wireless power transfer for smart power distribution in a miniature-sized multiple-receiver system,” *IEEE Trans. Ind. Electron.*, vol. 63, no. 3, pp. 1853–1862, Mar. 2016.

[11] D. Thenathayalan and J.-H. Park, “Individually regulated multiple-output WPT system with a single PWM and single transformer,” *IEEE J. Emerg. Sel. Topics Power Electron.*, vol. 8, no. 4, pp. 3542–3557, Dec. 2020.

[12] C. Qi, S. Huang, X. CHen, and P. Wang, “Multifrequency modulation to achieve an individual and continuous power distribution for simultaneous MR-WPT system with an inverter,” *IEEE Trans. Power Electron.*, vol. 36, no. 11, pp. 12440–12455, Nov. 2021.

[13] C. Qi, S. Huang, X. CHen, and P. Wang, “Individual output voltage regulation method of multifrequency multireceiver simultaneous WPT systems with a single inverter,” *IEEE J. Emerg. Sel. Topics Power Electron.*, vol. 11, no. 1, pp. 1245–1261, Feb. 2023.

[14] C. Xia, N. Wei, H. Zhang, S. Zhao, Z. Li, and Z. Liao, "Multifrequency and multiload MCR-WPT system using hybrid modulation waves SPWM control method," *IEEE Trans. Power Electron.*, vol. 36, no. 11, pp. 12400–12412, Nov. 2021.
[15] C. Xia et al., "Hybrid modulation PWM-controlled multifrequency and multiload WPT system based on variable resonant network," *IEEE Trans. Power Electron.*, vol. 39, no. 3, pp. 3873–3887, Mar. 2024.
[16] A. Sun et al., "Multifrequency and multiload MCR-WPT system based on hysteresis current control," *IEEE Trans. Power Electron.*, vol. 39, no. 8, pp. 10532–10545, Aug. 2024.
[17] C. Xia, Y. CHen, A. Sun, Y. Cao, X. Wang, and Q. Wang, "Switching frequency control strategy of inverter for multifrequency multiload WPT system based on hysteresis current control," *IEEE Trans. Power Electron.*, vol. 39, no. 10, pp. 13946–13961, Oct. 2024.
[18] A. Sun et al., "Parameter identification method for multifrequency and multiload MCR-WPT system based on hysteresis current control," *IEEE Trans. Power Electron.*, vol. 40, no. 9, pp. 12661–12675, Sep. 2025.
[19] Y. Liu, C. Liu, X. Gao, and S. Liu, "Design and control of a decoupled multichannel wireless power transfer system based on multilevel inverters," *IEEE Trans. Power Electron.*, vol. 37, no. 8, pp. 10045–10060, Aug. 2022.
[20] Z. Zhang, X. Li, H. Pang, H. Komurcugil, Z. Liang, and R. Kennel, "Multiple-frequency resonating compensation for multichannel transmission of wireless power transfer," *IEEE Trans. Power Electron.*, vol. 36, no. 5, pp. 5169–5180, May 2021.

Chenyang Xia (Member, IEEE) was born in Jiangsu Province, China, in 1982. He received the B.S., M.S., and Ph.D. degrees in control theory and control engineering from Chongqing University, Chongqing, China, in 2006, 2008, and 2010, respectively.

From 2018 to 2019, he was an Academic Visitor with the University of Auckland, Auckland, New Zealand. He is currently a Professor with the School of Electrical Engineering, China University of Mining and Technology, Xuzhou, China.

Tao Lu was born in Jiangsu Province, China, in 2001. He received the B.S. degree in electrical engineering and automation from Anhui University of Science and Technology, Chuzhou, China, in 2023. He is currently working toward the master's degree in electrical engineering with China University of Mining and Technology, Beijing, China.

His current research interest includes wireless power transmission technology.

Ganquan Cui received the B.S. degree in electrical engineering in 2023 from the China University of Mining and Technology, Xuzhou, China, where he is currently working toward the M.S. degree in electrical engineering with the School of Electrical Engineering.

His research interest includes wireless power transfer.

Anran Sun received the B.S. degree in electrical engineering and intelligent control with the School of Electrical and Control Engineering, Liaoning Technical University, Huludao, China, in 2019. He is currently working toward the Ph.D. degree in electrical engineering with the School of Electrical Engineering, China University of Mining and Technology, Xuzhou, China.

His research interest includes wireless power transfer.

Xinheng Li received the B.S. degree in electrical engineering in 2023 from China University of Mining and Technology, Xuzhou, China, where he is currently working toward the M.S. degree in electrical engineering with the School of Electrical Engineering.

Xirui Wang received the B.S. degree in electrical engineering in 2023 from China University of Mining and Technology, Xuzhou, China, where she is currently working toward the M.S. degree with the School of Electrical Engineering.

Her research interest includes wireless power transfer.

Yan Sun received the B.S. degree in electrical engineering from the Nanjing University of Information Science and Technology, Nanjing, China, in 2024. He is currently working toward the M.S. degree in electrical engineering with the School of Electrical Engineering, China University of Mining and Technology, Xuzhou, China.

His research interest includes wireless power transfer.